DOI: https://doi.org/10.2138/am-2018-6362

REVISION 2

Non-hydrostatic stress field orientation inferred from orthopyroxene (Pbca) to low-clinoenstatite ($P2_1/c$) inversion in partially dehydrated serpentinites

Maxime Clément (1), José Alberto Padrón-Navarta (1), Andréa Tommasi (1), David Mainprice (1)

(1) Géosciences Montpellier, CNRS & Univ. Montpellier, Montpellier, France

Submitted to American Mineralogist

Abstract

The direction of the main compressional stress, at the origin of the orthoenstatite (Oen) inversion to low-clinoenstatite (LCen) lamellae observed in partially dehydrated antigorite-serpentinites, has been inferred based on the crystallographic orientation relationship between Oen host crystals and the LCen lamellae by means of Electron Backscattered Diffraction (EBSD) combined with optical microscopy. This technique was applied to two samples: a transitional lithology (Atg-Chl-Ol-Opx) and a metaperidotite (Chl-Ol-Opx), both collected within 3 m from the serpentinite dehydration front exposed in Cerro del Almirez (Betic cordillera, South Spain). The metaperidotite displays a clear crystal preferred orientation (CPO) of both Oen and LCen. The transitional lithology shows weaker CPOs. The metaperidotite contains LCen crystals representative of two possible variants of the Oen to LCen martensitic transformation with distinct orientations, which are consistent with a unique compression direction at ca. 45° to the normal to the foliation and to the lineation of the precursor serpentinite. In contrast, in the transitional sample, calculated compressional stresses display an almost random orientation. The observation of such a variation in the stress field recorded by two samples separated by <3 m rules out a tectonic origin for the stresses producing the LCen in these metaperidotites. We interpret therefore these stresses as resulting from compaction during dehydration. The present analysis implies that these compaction-related stresses, though variable at the meter scale, may be organized at the cm scale during dehydration reactions of serpentinite.

Keywords: Clinoenstatite, stress field, martensitic transformation, serpentinite, dehydration reactions, non-hydrostatic stress

Introduction

Experimental work (Sclar et al. 1964; Boyd and England 1965; Grover 1972; Yamamoto and Akimoto 1977; Khodyrev and Agoshkov 1986; Angel et al. 1992; Wunder and Schreyer 1992, 1997; Luth 1995; Ulmer and Stalder 2001; Jahn and Martoňák 2009) provides evidence for the existence of several polymorphs of enstatite $MgSiO_3$ (Fig. 1): protoenstatite with a space group (*Pbcn*), orthoenstatite *Pbca* (Oen), a high-pressure clinoenstatite *C2/c* (HCen), a low-pressure high-temperature clinoenstatite *C2/c*, and a low pressure and low temperature clinoenstatite with a space group $P2_1/c$ (LCen). More recently, Zhang *et al.* (2012) discovered a second high-pressure clinoenstatite with the space group $P2_1/c$. Enstatite occurs in mantle and crustal rocks almost exclusively in the Oen form. LCen is known to occur in stony meteorites for some time, but its occurrence on Earth was not reported until the work of Dallwitz et al. (1966). Most terrestrial descriptions are related to volcanic rocks, which contain multiply twinned LCen (Dallwitz et al. 1966; Dietrich et al. 1978; Komatsu 1980; Shiraki et al. 1980; Yasuda et al. 1983). A minor proportion of described LCen crystals has a metamorphic or a deformational origin; these crystals are typically untwinned (Trommsdorff et al. 1968; Frost et al. 1978; Bozhilov et al. 1999; Ruiz Cruz et al. 1999; Padrón-Navarta et al. 2015; Zhang et al. 2017) . Twinned LCen in meteorites and in terrestrial rocks were interpreted to form by cooling from protoenstatite (Brown and Smith 1963; Boyd and England 1965; Yasuda et al. 1983), whereas untwinned LCen is interpreted to form by martensitic transformation from Oen due to shear on (100) planes in the [001] direction (Turner et al. 1960; Coe 1970; Raleigh et al. 1971; Coe and Muller 1973; Coe and Kirby 1975; Frost et al. 1978). Clinoenstatite with a space group $P2_1/c$ has also been described in peridotites from presumed ultra-high pressure origin such as Alpe Arami

(Bozhilov et al. 1999), Dabie-Sulu garnet pyroxenites (Zhang et al. 2002), Indus ophiolite (Das et al. 2015) and in the Luobusa ophiolite (Zhang et al. 2017). In these cases, the occurrence of LCen was interpreted as the result of decompression from the stability field of HCen with a space group *C*2/*c* (Fig. 1), implying exposure of these rocks to ultrahigh pressures >10 GPa corresponding to more than 300 km depth, although a martensitic transformation from Oen can not be discarded.

Coe and Muller (1973) established experimentally the relation between the Oen/LCen crystallographic orientations and the sense of shear during the transformation (Fig. 2), providing a potential technique to infer the orientation of the principal stresses in a similar way to the analysis of calcite, diopside, and plagioclase mechanical twins (e.g. Turner, 1953; Raleigh and Talbot, 1967, Egydio-Silva and Mainprice, 1999). The study of Frost et al. (1978) was the first one (and the last, to our knowledge) to apply this method. They analyzed a metaperidotite produced by serpentine dehydration in the Mount Stuart Batholith in the Central Cascades of Washington and determined that orientation of Oen host crystals containing LCen lamellae measured by universal stage differed significantly from the Oen bulk fabric in the metaperidotite. Based on these data, they suggested that the Oen to LCen inversion was unrelated to the dehydration event and most likely caused by stresses related to the activity of a nearby shear zone.

The recent description of LCen lamellae in Oen in Cerro del Almirez metaperidotites (Padrón-Navarta et al. 2015) opens the possibility to investigate the Oen-LCen inversion in the context of a near-hydrostatic dehydrating system. These metaperidotites formed by serpentine dehydration at high-pressure conditions (eclogite facies, López Sánchez-Vizcaíno et al. 2005, Padrón-Navarta et al. 2010a, Fig.1). They display no evidence of tectonic deformation after the dehydration event consistently with the absence of macroscopic shear zones within the metaperidotite part of this unit. However, they show microstructures indicative of grain-scale deformation in response to compaction of the fluid-filled porosity produced by the serpentine dehydration reaction, which may reach ca. 20 vol. % (Padrón-Navarta et al. 2015). Compaction of a transient fluid-filled porosity produced by dehydration reactions should be associated with a complex stress field with variable orientation and magnitude at the grain scale (Wheeler 1987; Llana-Fúnez et al. 2012). The analysis of the orientation of LCen lamellae in the Cerro del Almirez peridotites allow testing this model by constraining the orientation of compressional stresses during porosity compaction. This work presents the first Electron Backscattered Diffraction (EBSD) study of the Oen to LCen inversion. Based on these data, we discuss the mechanisms of Oen transformation to LCen and the origin of the stresses responsible for this phase transformation in the Cerro del Almirez metaperidotites.

Strategy and Methods

Geological background and samples selection

The Cerro del Almirez (Nevado–Filábride Complex, Betic Cordillera, SE Spain) displays an undisturbed serpentine dehydration front, in which antigorite-schists are transformed to chlorite-harzburgites with granofels and spinifex-like textures (Trommsdorff et al. 1998; Garrido et al. 2005; López Sánchez-Vizcaíno et al. 2005, 2009, Padrón-Navarta et al. 2008, 2010a, 2011, 2015; Kahl et al. 2017). The reaction occurred at 680-710°C and 1.6-1.9 GPa (Fig.1) (López Sánchez-Vizcaíno et al., 2005, Padrón-Navarta et al., 2010a) during subduction of the Nevado-Filábride Complex in the Middle Miocene (López Sánchez-Vizcaíno et al. 2001). Later extensional tectonics resulted in exhumation of the reaction front (Martinez-Martinez et al., 2002), but this deformation was localized along the contacts of the ultramafic bodies with the metapelites and did not affect the internal parts of the ultramafic bodies (Jabaloy et al. 2015). The penetrative foliation of the antigorite serpentinite protolith is obliquely crosscut by the irregularly shaped reaction front marked by growth of the prograde assemblage (olivine + enstatite + chlorite +/- tremolite), suggesting that the dehydration reactions producing the clinoenstatite-bearing metaperidotites occurred under nearly static conditions (Padrón-Navarta et al., 2011, 2015).

In this study, we analyse the orientation of Oen and LCen in two samples from Cerro del Almirez: an antigorite-bearing transitional lithology (sample Al10-10, antigorite present), a chlorite-serpentinite collected ca. 70 cm away from the first isograd of the dehydration reaction, which is marked by the growth of coarse-grained chlorite, and an antigorite-absent chlorite-harzburgite with granofels texture collected ca. 3 m away from the same isograd (Al10-11, Fig. 3) (Padrón-Navarta et al. 2015). These two samples are oriented in a similar way and are distant by <2,5 m. The composition of orthopyroxene in both transitional and granofels texture metaperidotite is typically low in aluminium (0.10 wt. % Al_2O_3) with an X_{Mg} (Mg/(Fe^{2+}+Mg) of 0.90-0.91 (Padrón-Navarta et al. 2011). Because LCen lamellae are only visible optically when the Oen [010] axis is at high angle to the thin section plane (see later discussion), four oriented sections - two XZ sections (A_1 and A_2), one XY (B), and one YZ (C) section, where X defines the lineation and Z the normal to the foliation plane - were analyzed for each sample.

In addition, we performed detailed observations of a large bent Oen crystal (4 mm in length) from a coarse grained chlorite-harzburgite with granofels texture (Al09-16) collected at 25 m from the reaction front. The continuous and strong variation of the orientation of the host Oen crystal allowed us to test the relation between the sense of the shear during the LCen martensitic transformation and the orientation of the host Oen relative to the local stresses (Coe and Muller, 1973). Although chlorite-harzburgites with pseudospinifex texture also contain nanometer size LCen (Ruiz-Cruz et al. 1999), metaperidotites with this texture were not investigated, since the LCen lamellae in these peridotites are below both optical and EBSD resolution.

Analytical techniques

We performed EBSD analyses at Géosciences Montpellier (France). We used a Camscan Crystal Probe XF500 with a EBSD HKL NordlysNano detector to measure the crystallographic orientation of the LCen lamellae and a JEOL 5600 with a EBSD NordlysNano detector to map the orientation of Oen with a resolution of 16-27 μm over the whole thin section. In order to obtain the clearest Kikuchi patterns, the binning mode was set to 2x2 for both spot analyses and orientation mapping of small areas containing LCen lamellae (Table 1). Frame averaging was set to 2 to decrease noise. Reference LCen diffraction patterns were indexed using the crystallographic data of Morimoto *et al.*, (1960) with a=9.620 Å, b=8.825 Å, c=5.188 Å, and β = 71.67°, because these parameters resulted in the best fit of the observed patterns, producing Mean Angular Deviation (MAD) values ≤ 0.50° (Table 1). For further treatment, we transformed the LCen orientations to the conventional monoclinic setting (Fig. 2, β = 108.33°; Ohashi, 1984) by adding 180° to the third Bunge Euler angle.

Apparent thickness of LCen lamellae varies from <1 μm to 50 μm. This implies in EBSD measurements steps of 0.2-0.5 μm and makes EBSD mapping of the whole thin section too time consuming. Therefore crystals of Oen containing LCen were first identified by optical microscopy and then the orientation of both Oen host and LCen host was measured by EBSD using either spot analysis or small-scale maps. We successfully indexed more than 84% of the optically identified LCen crystals despite the small size of the lamellae.

This grain-by-grain analysis is also time consuming. To enhance the statistics, we used a mixed EBSD-optical technique, in which the orientation of LCen crystals was calculated from the host Oen crystal determined by EBSD mapping and the phase transformation variant (dextral or sinistral shearing, Fig. 2) was identified by optical microscopy. Optical microscopy observations under crossed-polarized light allow the determination of the relative orientation of the γ-optical axis of LCen relatively to the host Oen (i.e. right or left LCen extinction relative to the [001] Oen/LCen direction, Coe and Muller, 1973). Since the LCen γ-optical axis is at 32° to [001] and lies in the obtuse angle [100]^[001] in the monoclinic setting of Ohashi (1984) (Fig. 2), knowledge of the orientation of this optical axis allows the determination of the full orientation of the LCen crystal and therefore the orientation of the main compressional stress. The number of Oen crystals hosting LCen lamellae identified in each thin section, as well as the proportions of the two LCen variants are listed in Table 1.

Orientation data for both LCen and Oen were analyzed using MTEX (Hielscher & Schaeben, 2008, Bachmann et al., 2010;; Mainprice et al., 2014). They are displayed as pole figures in the XYZ reference frame, which is based on the orientation of the foliation and lineation of the precursor serpentinite. The calculated LCen orientations based on the orientations of the measured host Oen orientations given by EBSD data and optical determinations of the variant selection are consistent with the EBSD data of LCen for both samples (Fig. 4). This validates the mixed

EBSD-optical approach, which is considerably faster than the LCen EBSD analysis. In addition, to evaluate what would be the LCen population if all Oen crystals in the rock contained LCen lamellae, we wrote a MTEX script, which, based on the theoretical transformation relation (Fig. 2), converted the Oen orientations measured over the entire thin section by EBSD mapping into LCen orientations with a random variant choice. When the orientation of LCen is measured by EBSD, the type of variant and the orientation of the main compressional stress (σ_1) for each Oen grain hosting LCen is uniquely determined. The orientation of σ_1 can be then computed, for instance, by a 45° clockwise rotation of the orientation data for LCen around the positive $[010]_{LCen}$ axis (c.f. Fig. 2, note that in this figure the positive $[010]_{LCen}$ axis points away from the viewer in case of variant 1). The orientation of σ_1 is parallel to the orientation of $[001]_{LCen}$ of the rotated data. More generally, however, the orientation of σ_1 can be determined by knowing (1) the orientation of the Oen host and (2) the type of LCen variant, which can be obtained by optical microscopy. Because two crystallographically opposite orientations of $[010]_{Oen}$ are compatible for each type of LCen variant (only the one with $[010]_{Oen}$ away from the viewer is represented in Fig. 2), the sign of rotation (clockwise or anticlockwise) depends on the orientation of the positive $[010]_{Oen}$ axis. A simple MTEX Matlab script is provided as Appendix to compute the orientation of σ_1 based exclusively on the orientation data for Oen and the type of LCen variant.

Results

Low-clinoenstatite optical features

In optical microscopy with cross-polarized light, LCen lamellae generally appear as light to dark grey <1 µm to up to 50 µm wide elongated bands within the Oen crystals

(Fig. 5a). Sample Al09-16 contains a large bent Oen grain hosting LCen lamellae, whose extinction position changes abruptly across the microfold hinge, indicating a change in phase transition variant (Fig. 2) in response to the change in the orientation of the Oen crystal relative to the main compressive stress (Fig. 5a). EBSD orientation mapping validates this interpretation (Figs. 5b and c). Comparison of Kikuchi patterns from the Oen host and both LCen lamellae highlights that they differ by the aspect of the (121) band, which is composite for Oen, but single and thick in LCen, with asymmetric contrast for the two variants (Fig. 5c).

Oen and LCen orientation distributions

Projection of all Oen orientations obtained by EBSD mapping of the whole thin section for the antigorite-present sample Al10-10 and for the antigorite-absent sample Al10-11 reveals a weak but consistent crystal preferred orientation (CPO) characterized by [100] axes dominantly at low angle to the normal to the foliation (Z) and [001] axes forming a wide girdle at low angle to the foliation XY plane (Fig. 6a). In Al10-10, [010] axes are highly dispersed, but in Al10-11 they form a weak maximum at low angle to the Y direction.

Orientation data from EBSD spot analyses of LCen-hosting Oen crystals shows a consistent, but apparently stronger crystal preferred orientation (Fig. 6a,b), probably due to the smaller number of grains analyzed and the biasing effect of optical identification of LCen (see below).-Oen and LCen have subparallel [010] and [001] axes. The [010] directions tend to concentrate parallel to the structural Y direction, whereas [001] is dispersed at low angle to the XZ plane, with a weak concentration subparallel to X in sample Al10-11. Analysis of LCen data for sample Al10-11 highlights that the two LCen variants have significantly different orientations, with concentration of [100] axes at low angle to the Z direction for the variant 1 and close to the X direction for variant 2 (Fig. 6c). This phenomenon is less marked in sample Al10-10, maybe because of the lower number of LCen-bearing Oen crystals observed in this sample. In sample Al10-11, the population of variant 1 is slightly more abundant than the variant 2 one; it represents 66% of measured data in this section (Table 1).

Correcting for bias in LCen optical detection

LCen lamellae are only visible optically when their [010] axis is nearly parallel to the microscope axis. Thus the thin sections studied may have LCen that are not detectable optically. Calculation of the angle between [010] axes of measured and calculated LCen data and the normal to the thin section show that observed LCen-bearing Oen grains have their [010] axes within 50° of the normal to the thin section (Fig. 7). This may result in bias in the estimation of main compressive stress direction. To minimise this bias, orientation analyses were performed on 3 orthogonal sections (Fig. 8). LCen orientations derived from these additional sections (Fig. 8) are consistent with those in Fig. 6, in particular for the antigorite-absent sample (Al10-11). For the antigorite-present sample Al10-10, despite doubling the number of measurements, no clear preferred orientation of the two variants can be defined.

Compressional stress orientation

Main compressional stresses (σ_1) calculated based on LCen orientation data in the antigorite-present sample Al10-10 shows no clear preferred orientation, except for a weak maximum normal to the foliation, which is mainly derived from the data from the A_1 section (Fig. 8a). In contrast, main compressional stresses calculated for the antigorite-absent sample Al10-11 show a marked preferred orientation in the XZ plane, between 0-90° clockwise from the X direction, with a maximum at 49° of the foliation plane. It is noteworthy that the orientation data from the two variants add up consistently for the definition of a single stress orientation.

To evaluate what would be the predicted main compressive stress orientation if all Oen grains in the two samples were LCen-bearing, we estimated the associated LCen orientations considering a random variant selection. Both datasets result in a very weak orientation of the main compressive stress, which is almost random for sample Al10-10 (Fig. 8a) and forms a wide girdle at high angle to the Y direction for sample Al10-11 clearly differing from the prediction based on the measured LCen orientations (Fig. 8b).

Discussion

Stress-induced Oen to LCen inversion

The present microstructural observations clearly point to the formation of LCen lamellae by martensitic transformation of Oen. A key observation is the occurrence of LCen lamellae in sample Al09-16 with two different extinctions in a single large bent Oen grain (Fig. 5), which suggests that projection of the local stress on the two fold limbs gives rise to shear stresses with opposite senses leading to development of different LCen variants in the two fold limbs.

Peak metamorphic conditions, which led to dehydration of the serpentinite and formation of the host Oen crystals in the Cerro del Almirez metaserpentinites, are estimated at 1.6-1.9 GPa and temperatures of 680-710°C (Fig. 1) (Padrón-Navarta *et al.*, 2010a, 2011). These conditions are within the Oen field according to the phase diagram of Ulmer and Stalder (2001), which was based on experiments on

DOI: https://doi.org/10.2138/am-2018-6362

orthopyroxenes with compositions ranging from pure enstatite (Mg# = 1,00) to 10% ferrosilite (Mg# =0.90), that is, for compositions similar to those of the studied samples (Mg# = 0.89-0.90). The phase transition between LCen and Oen is, however, displaced to higher temperatures if shear stresses are applied in the [001] direction on (100) planes of orthoenstatite (Coe, 1970). Because of the different nature and rheology of neighboring grains and, more important, of the reduced solid-solid contact points in the presence of porosity, a heterogeneous stress field, with locally high stresses, might form during compaction of porosity (e.g. Llana-Fúnez *et al.*, 2012). Such stresses may induce the phase transition from Oen to LCen at lower pressures than those predicted for static conditions. Padrón-Navarta *et al* (2015) estimated the magnitude of the stresses required to trigger orthoenstatite inversion at the peak conditions recorded by the Chl-harzburgite with granofels texture in Cerro Almirez based on the coexistence of plastic deformation microstructure in Oen hosts and coeval Oen inversion to LCen (Fig. 5) following the approaches of Raleigh et al. (1971) and Coe and Kirby (1975). Estimated differential stresses are on the order of 5-70 MPa.

The most favorable orientation for promoting the transformation of Oen to LCen is when the compression is applied at 45° from [100] and [001] axes, since this results in the highest shear stresses on (100) planes, allowing the transformation to occur at minimum compressive stress levels. The present calculations of the maximum compressive stress orientation are based on this assumption.

The two samples, which are separated by less than 2.5 m, have recorded different stress fields (Fig. 8a,b). Such short wavelength changes in the stress field are not compatible with a tectonic origin related to subduction or to the exhumation of the massif. This further corroborates the hypothesis that the stresses producing the

Oen to LCen transformation were associated with the compaction of the fluid-filled porosity produced by the antigorite dehydration.

The consistent orientation of the maximum compressive stress from the two variant populations of LCen in the antigorite-absent sample Al10-11 indicates that two populations of Oen with markedly different orientations have recorded the same orientation of compressional stress (Fig. 6c, Fig. 8b). This observation implies a homogeneous stress field at the thin section (cm) scale and is at odds with the strong variations in the compressive stress orientation at the grain-scale modelled by Llana-Fúnez *et al* (2012). A highly variable orientation of the maximum compressional stress applied on an Oen population with strong CPO would result in a lack of clear orientation distribution of the two LCen variant populations, as predicted for the antigorite-present sample Al10-10 and for the calculations in which we considered that all Oen in the sections were LCen-bearing (Fig. 8a).

Spatial variation of the stress field and compaction scales

The variation in degree of dehydration and in the associated porosity could be at the origin of the differences in the stress field between the two samples. The antigorite-present sample Al10-10 was only partially dehydrated. Lack of or incomplete fluid extraction at this early stage of the process might have resulted in a small region of solid grain-to-grain contacts and in an increase of the hydrostatic component, producing a highly heterogeneous stress field with no macroscopic preferred orientation of σ_1, similar to the one modeled by Wheeler (1987, see also Fig 1 in Llana-Fúnez *et al* 2012). The antigorite-absent sample Al10-11, on the other hand, records a more developed stage of the process, in which fluid extraction by compaction and porosity collapse might have resulted in a more homogeneous stress field. Macroscopic (> 1-2 cm) diffuse shear zones that might be related to the compaction processes are observed in this sample (Fig. 3b), pointing to a coherent stress field at the sample scale.

The compaction length scale (δ, in m) during dehydration reactions is the deformation length scale over which pore fluids are at hydrostatic pressure and can move independently of the compaction process. It can be expressed as (Connolly 1997, 2010):

$$\delta \approx \sqrt{\frac{3}{4}\frac{\eta}{\mu}\frac{k}{\phi}} , \quad (1)$$

where k is the permeability, μ is the fluid viscosity (10^{-4} Pa·s, Connolly 1997), η is the dynamic viscosity, and ϕ is the porosity. The viscosity of serpentinite before dehydration at the temperature and pressure of interest (680°C and 1.7 GPa) is 4.0×10^{20} Pa·s for a shear stress of 1 MPa (using the power law equation of Hilairet et al. 2007), which is in the same range as the estimated viscosity of the fluid-bearing metaperidotites during the compaction process (1.0×10^{20} Pa·s at 680°C for a shear stress of 70 MPa, Padrón-Navarta et al. 2015). Therefore the evolution of the compaction scale during the dehydration processes is expected to be influenced by the relative changes in the ratio of k/ϕ during dehydration rather than by contrasting viscosities between the serpentinite and compacting metaperidotite. This is supported by the limited macroscopic perturbation of the dehydration front and the serpentinite foliation plane during the dehydration event (Fig. 3).

Direct experimental measurements of permeability and porosity in serpentinite are only available at 50 MPa (Kawano et al., 2011, Katayama et al., 2012). Extrapolation to higher pressure (1.7 GPa) following the approach used by Kawano et al. (2011) results in extremely low permeability perpendicular to foliation (3.5×10^{-27}

m^2). Assuming this porosity (k) and using the theoretical approach of Gueguen and Palciauskas (1994), which considers cylindrical tube channels, to relate permeability and porosity:

$$k = k_0 \left(\frac{\phi}{\phi_0}\right)^2, \quad (2)$$

the porosity (ϕ) in the serpentinite at 1.7 GPa before dehydration is also estimated to be very low (0.002 %), using the reference permeability (k_0) and porosity (ϕ_0) values at 50 MPa (Kawano et al. 2011).

During the initial stages of dehydration (represented by the antigorite-present sample Al10-10), the increase in porosity would lead to an increase in compaction length compatible with the near-hydrostatic stress recorded in this sample. An increase in porosity by three orders of magnitude (up to 2 %) relative to the background porosity in the serpentinite as a consequence of solid volume reduction during the reaction would result in a compaction length in the order of 150m using Eq. (1) and (2). The observation of non-hydrostatic stresses in the antigorite-absent sample Al10-11 suggests that porosity reduction due to fluid extraction resulted in significantly smaller compaction lengths. The poor knowledge of the quantitative relationship between permeability and porosity during the reaction progress makes quantifying the reduction in the compaction length challenging. However, the observed meter-scale variation in stress distribution (interpreted as a change from hydrostatic to non-hydrostatic conditions) requires a reduction in compaction length equivalent to the one that might be produced by a decrease in porosity by two orders of magnitude, that is, almost complete fluid extraction.

Implications

The present observations imply that compaction during dehydration of serpentinites may generate differential stresses on the order of several tens of MPa. These stresses might be recorded by shear-induced phase transformations such as the inversion of orthoenstatite produced by the dehydration reaction to low-clinoenstatite. The present observations, which record variable stress fields in two samples separated by <3 m and recording different stages of the reaction, suggest that the stress field varies both in time and space in response to the reaction progress and evolution of compaction. At the initial stages of the reaction, when porosity is high and most grain-boundaries are wet (reducing solid-solid contacts) the system behaves as near-hydrostatic and compaction length-scales are large (hundreds of meters). When reaction progresses, decrease in porosity reduces the compaction length to the meter scale and compaction may organize the stress field. This might influence fluid migration resulting in macroscopic compaction structures (from dm to m) that can be potentially identified in the field in the absent of post-dehydration deformation.

Acknowledgements

We are grateful to F. Barou for his technical assistance in the EBSD-SEM CNRS-INSU national facility at Géosciences Montpellier. We acknowledge C. J. Garrido and V. López Sánchez-Vizcaíno for constructive discussions , Rüdiger Kilian and Ralf Hielscher for suggestions to improve MTEX scripts and the reviewer for his relevant comments and remarks. C. Nevado and D. Delmas supplied high quality polished thin sections for EBSD measurements. This work has been funded by a PhD grant (GAIA, Université Montpellier) to M.C. and by the CNRS-INSU (TelluS/SYSTER) project MinCompact (AO2017-996352).

References

Angel, R.J., Choplelas, A., and Ross, N.L. (1992) Stability of high-density clinoenstatite at upper-mantle pressures. Nature, 358, 322–324.

Bachmann, F., Hielscher, R., Jupp, P.E., Pantleon, W., Schaeben, H., and Wegert, E. (2010) Inferential statistics of electron backscatter diffraction data from within individual crystalline grains. Journal of Applied Crystallography, 43, 1338–1355.

Boyd, F.R., and England, J.L. (1965) The rhombic enstatite-clinoenstatite inversion. Carnegie Institution Yearbook, 64, 117–120.

Bozhilov, K.N., Green II, H.W., and Dobrzhinetskaya, L. (1999) Clinoenstatite in Alpe Arami Peridotite: Additional Evidence of Very High Pressure. Science, 284, 128–132.

Brown, W.L. and Smith, J.V. (1963) High-temperature x-ray studies on the polymorphism. Zeitschrift fur Kristallographie, 212, 186–212.

Coe, R.S. (1970) The thermodynamic effect of shear stress on the ortho-clino inversion in enstatite and other coherent phase transitions characterized by a finite simple shear. Contributions to Mineralogy and Petrology, 26, 247–264.

Coe, R.S., and Kirby, S.H. (1975) The Orthoenstatite to Clinoenstatite Transformation by Shearing and Reversion by Annealing: Mechanism and Potential Applications. Contributions to Mineralogy and Petrology, 52, 29–55.

Coe, R.S., and Muller, W.F. (1973) Crystallographic orientation of clinoenstatite produced by deformation of orthoenstatite. Science, 180, 64–66.

Connolly, J. A. D. (1997) Devolatilization-generated fluid pressure and deformation-propagated fluid flow during prograde regional metamorphism. Journal of Geophysical Research, 102, 149-173.

Connolly, J. A D. (2010) The mechanics of metamorphic fluid expulsion. Elements, 6, 165–172.

Dallwitz, W.B., Green, D.H., and Thompson, J.E. (1966) Clinoenstatite in a volcanic rock from the cape vogel area, papua. Journal of Petrology, 7, 375–403.

Das, S., Mukherjee, B.K., Basu, A.R., and Sen, K. (2015) Peridotitic minerals of the Nidar Ophiolite in the NW Himalaya: sourced from the depth of the mantle transition zone and above. Geological Society, London, Special Publications, 412, 271–286.

Dietrich, V., Emmerman, R., Oberhänsli, R., and and Puchelt, H. (1978) Geochemistry of basaltic and gabbroic rocks from the west Mariana trench. Earth and Planetary Science Letters, 39, 127–144.

Frost, B.R., Coe, R.S., and Okamura, F.P. (1978) Principal stress directions from a natural occurrence of stress-induced clinoenstatite. Contributions to Mineralogy and Petrology, 67, 119–126.

Garrido, C.J., Sánchez-Vizcaíno, V.L., Gómez-Pugnaire, M.T., Trommsdorff, V., Alard, O., Bodinier, J.L., and Godard, M. (2005) Enrichment of HFSE in chlorite-harzburgite produced by high-pressure dehydration of antigorite-serpentinite: Implications for subduction magmatism. Geochemistry, Geophysics, Geosystems, 6, Q01J15.

Gasparik, T. (2014) Phase Diagrams for Geoscientists. An Atlas of the Earth's Interior, 462 p.

Grover, J. (1972) The stability of low-clinoenstatite in the system Mg2Si2 O6 -CaMgSi2O6, Transactions of the American Geophysical Union, 53:539.

Hielscher, R., and Schaeben, H. (2008) A novel pole figure inversion method: specification of the *MTEX* algorithm. Journal of Applied Crystallography, 41, 1024–1037.

Jabaloy-Sánchez, A., Gómez-Pugnaire, M.T., Padrón-Navarta, J.A., López Sánchez-Vizcaíno, V., and Garrido, C.J. (2015) Subduction- and exhumation-related structures preserved in metaserpentinites and associated metasediments from the Nevado-Filábride Complex (Betic Cordillera, SE Spain). Tectonophysics, 644, 40–57.

Jahn, S., and Martoňák, R. (2009) Phase behavior of protoenstatite at high pressure studied by atomistic simulations. American Mineralogist, 94, 950–956.

Kahl, W.-A., Dilissen, N., Hidas, K., Garrido, C.J., López-Sánchez-Vizcaíno, V., and Román-Alpiste, M.J. (2017) 3-D microstructure of olivine in complex geological materials reconstructed by correlative X-ray μ-CT and EBSD analyses. Journal of Microscopy, 0, 1–15.

Kawano, S., Katayama, I., and Okazaki, K. (2011) Permeability anisotropy of serpentinite and fluid pathways in a subduction zone. Geology, 39, 939–942.

Khodyrev, O.Y., and Agoshkov, V.M. (1986) Phase transitions in serpentine in the MgO-SiO2 -H2 O system at 40–80 kbar. Geochemistry International, 23, 47–52.

Komatsu, M. (1980) Clinoenstatite in volcanic rocks from the Bonin Islands. Contributions to Mineralogy and Petrology, 74, 329–338.

Llana-Fúnez, S., Wheeler, J., and Faulkner, D.R. (2012) Metamorphic reaction rate controlled by fluid pressure not confining pressure: implications of dehydration experiments with gypsum. Contributions to Mineralogy and Petrology, 164, 69–79.

López Sánchez-Vizcaíno, V., Rubatto, D., Gómez-pugnaire, M.T., Trommsdorff, V., and Müntener, O. (2001) Middle Miocene high-pressure metamorphism and fast exhumation of the Nevado- Filabride Complex , Terra Nova, 13, 327-332.

López Sánchez-Vizcaíno, V., Trommsdorff, V., Gómez-Pugnaire, M.T., Garrido, C.J., Müntener, O., and Connolly, J.A.D. (2005) Petrology of titanian clinohumite and olivine at the high-pressure breakdown of antigorite serpentinite to chlorite harzburgite (Almirez Massif, S. Spain). Contributions to Mineralogy and Petrology, 149, 627–646.

López Sánchez-Vizcaíno, V., Gómez-Pugnaire, M.T., Garrido, C.J., Padrón-Navarta, J.A., and Mellini, M. (2009) Breakdown mechanisms of titanclinohumite in antigorite serpentinite (Cerro del Almirez massif, S. Spain): A petrological and TEM study. Lithos, 107, 216–226.

Luth, R.W. (1995) Is phase A relevant to the Earth's mantle? Geochimica et Cosmochimica Acta, 59, 679–682.

Mainprice, D., Bachmann, F., Hielscher, R., and Schaeben, H. (2014) Descriptive tools for the analysis of texture projects with large datasets using MTEX: strength, symmetry and components. Geological Society, London, Special Publications, 409, 251-271.

Martinez-Martinez, J.M., Soto, J.I., and Balany, J.C. (2002) Orthogonal folding of extensional detachments: Structure and origin of the Sierra Nevada elongated dome (Betics, SE Spain). Tectonics, 21, 1-20.

Morimoto, N., Appleman, D.E., and Evans, H.T. (1960) The crystal structures of clinoenstatite and pigeonite. Zeitschrift fur Kristallographie, 147, 120–147.

Ohashi, Y. (1984) Polysynthetically-twinned structures of enstatite and wollastonite. Physics and Chemistry of Minerals, 10, 217–229.

Padrón-Navarta, J.A., Hermann, J., Garrido, C.J., López Sánchez-Vizcaíno, V., and Gómez-Pugnaire, M.T. (2010a) An experimental investigation of antigorite dehydration in natural silica-enriched serpentinite. Contributions to Mineralogy and Petrology, 159, 25–42.

Padrón-Navarta, J.A., Tommasi, A., Garrido, C.J., Sánchez-Vizcaíno, V.L., Gómez-Pugnaire, M.T., Jabaloy, A., and Vauchez, A. (2010b) Fluid transfer into the wedge controlled by high-pressure hydrofracturing in the cold top-slab mantle. Earth and Planetary Science Letters, 297, 271–286.

Padrón-Navarta, J.A., Sánchez-Vizcaí, V.L., Garrido, C.J., and Gómez-Pugnaire, M.T. (2011) Metamorphic record of high-pressure dehydration of antigorite serpentinite to chlorite harzburgite in a subduction setting (Cerro del Almirez, Nevado-Filábride complex, Southern Spain). Journal of Petrology, 52, 2047–2078.

Padrón-Navarta, J.A., Tommasi, A., Garrido, C.J., and Mainprice, D. (2015) On topotaxy and compaction during antigorite and chlorite dehydration: an experimental and natural study. Contributions to Mineralogy and Petrology, 169, 1-20.

Padrón-Navarta, J. A., López Sánchez-Vizcaíno, V., Garrido, C.J., Gómez-Pugnaire, M.T., Jabaloy, a., Capitani, G.C., and Mellini, M. (2008) Highly ordered antigorite from Cerro del Almirez HP-HT serpentinites, SE Spain. Contributions to Mineralogy and Petrology, 156, 679–688.

Raleigh, C. B. and Talbot, J.L. (1967) Mechanical twinning in naturally and experimentally deformed diopside. American Journal of Science, 265, 151–165.

Raleigh, C.B., Kirby, S.H., Carter, N.L., and Lallemant, H.G.A. (1971) Slip and the clinoenstatite transformation as competing rate processes in enstatite. Journal of

Geophysical Research, 76, 4011–4022.
Ruiz Cruz, M.D., Puga, E., and Nieto, J.M. (1999) Silicate and oxide exsolution in pseudo-spinifex olivine from metaultramafic rocks of the Betic ophiolitic association: A TEM study. American Mineralogist, 84, 1915–1924.
Sclar, C.B., Carrison, L.C., and Schwartz, C.. (1964) High pressure stability fields of clinoenstatite, and the orthoenstatite- clinoenstatite transition. EOS, Transactions of the American Geophysical Unionactions of the American Geophysical Union, 45:121.
Shiraki, K., Kuroda, N., Nurano, H., and Maruyama, S. (1980) Clinoenstatite in volcanic rocks from the Bonin Islands, Japan. Nature, 285, 30–32.
Trommsdorff, H., Baker, V., and David, W. (1968) Inverse pole-figures of two carbonate fabrics, Schweizerische Mineralogische Und Petrographische Mitteilungen, 48, 467-470.
Trommsdorff, V., and Wenk, H.R. (1968) Terrestrial metamorphic clinoenstatite in kinks of bronzite crystals. Contributions to Mineralogy and Petrology, 19, 158–168.
Trommsdorff, V., Sanchez-Vizcaino, V.L., Gomez-Pugnaire, M.T., and Muntener, O. (1998) High pressure breakdown of antigorite to spinifex-textured olivine and orthopyroxene, SE Spain. Contributions to Mineralogy and Petrology, 132, 139–148.
Turner, F.J. (1953) Nature and dynamic interpretation of deformation lamellae in calcite of three marbles. American Journal of Science, 251, 276-298.
Turner, F.J., Heard, H., and Griggs, D.T. (1960) Experimental deformation of enstatite and accompanying inversion to clinoenstatite. Report of 21st International Geological Congress, Copenhagen, 18, 399–408.
Ulmer, P., and Stalder, R. (2001) The Mg (Fe) SiO3 orthoenstatite-clinoenstatite transitions at high pressures and temperatures determined by Raman-spectroscopy on quenched samples. American Mineralogist, 86, 1267–1274.
Wheeler, J. (1987) The significance of grain scale stresses in the kinetics of metamorphism. Contributions to Mineralogy and Petrology, 97, 397–404.
Wunder, B., and Schreyer, W. (1992) Metastability of the 10-A phase in the system MgO-SiO2-H2O (MSH). what about hydrous MSH phases in subduction zones? Journal of Petrology, 33, 877–889.
——— (1997) Antigorite: High-pressure stability in the system MgO-SiO2-H2O (MSH). Lithos, 41, 213–227.
Yamamoto, K., and Akimoto, S. (1977) The system MgO-SiO 2 -H 2 O at high pressures and temperatures; stability field for hydroxyl-chondrodite, hydroxyl-clinohumite and 10 A o -phase. American Journal of Science, 277, 288-312.
Yasuda, M., Kitamura, M., and Morimoto, N. (1983) Electron microscopy of clinoenstatite from a boninite and a chondrite. Physics and Chemistry of Minerals, 9, 192–196.
Zhang, J.S., Dera, P., and Bass, J.D. (2012) A new high-pressure phase transition in natural Fe-bearing orthoenstatite. American Mineralogist, 97, 1070–1074.
Zhang, R.Y., Shau, Y.H., Liou, J.G., and Lo, C.H. (2002) Discovery of clinoenstatite in garnet pyroxenites from the Dabie-Sulu ultrahigh-pressure terrane, east-central China. American Mineralogist, 87, 867–874.
Zhang, R.Y., Shau, Y.H., Yang, J.S., and Liou, J.G. (2017) Discovery of clinoenstatite in the Luobusa ophiolitic mantle peridotite recovered from a drill hole, Tibet. Journal of Asian Earth Sciences, 145, 605-612.

APPENDIX

```
% MTEX version 4.5.2
%14/02/2018
```

This is a preprint, the final version is subject to change, of the American Mineralogist (MSA)
Cite as Authors (Year) Title. American Mineralogist, in press.
DOI: https://doi.org/10.2138/am-2018-6362

```
% Script written by Maxime Clément, Géoscience Montpellier, France.
%contact= maxime.clement@gm.univ-montp2.fr
clear all
close all
% define Oen crystal symmetry
cs = crystalSymmetry('mmm', [18.2406 8.8302 5.1852]);
%**********************************************************************
%% Example: define Oen Euler angles and variant vectors
%**********************************************************************
% Euler angles
E1=[0.8 177.6 173.3];
E2=[100.9 79.3 78.5];
E3=[0.9 179.2 0.4];
% variant vector
Var=[2 2 1];
% all 3 Oen orientations
ori=orientation('Euler',E1*degree,E2*degree,E3*degree,cs);
%**********************************************************************
%% compute the orientation of sigma
%**********************************************************************
% Define b-axes orientations of Oen
% positive and negative values plot in upper and lower
% hemisphere
% 3 orientations of Oen [010] in specimen coordinates
B=ori*Miller(0,1,0,cs,'uvw');%define b-axes of orthoenstatite as vectors
% calculation of sigma is done by rotating 45 degrees
% the Bunge Euler angles of Oen around around b-axis,
% For variant 1, rotation is + if B is +
% For variant 1, rotation is - if B is -
% For variant 2, rotation is - if B is +
% For variant 2, rotation is + if B is -
%
% Selection proceedure
for i=1:length(E1)
    if B(i).z>0 && Var(i)==1 || B(i).z<0 && Var(i)==2
        ori(i)=ori(i)*orientation('axis', ...
            Miller(0,1,0,cs),'angle',45*degree);
    else
        ori(i)=ori(i)*orientation('axis', ...
             Miller(0,1,0,cs),'angle',-45*degree);
    end
end
%**********************************************************************
%% plot sigma
% Red = Oen [001] lower hemisphere  Oen [001] lower hemisphere
%**********************************************************************
figure
% plot convention X-axis to east
plotx2east
for i=1:length(E1)
    if Var(i)==1
        plotPDF(ori(i),Miller(0,0,1,cs,'uvw'),...
            'lower','MarkerColor','blue','MarkerSize',16)
        hold on
    else
        plotPDF(ori(i),Miller(0,0,1,cs,'uvw'),...
            'lower','MarkerColor'...
            ,'red','MarkerSize',16)
        hold on
    end
end
% figure title
a=annotation('textbox',[0.420 0.939 0.174 0.055],'String',...
    'Sigma','LineStyle','none','BackgroundColor','white');
a.FontSize=20;
a=annotation('textbox',[0.015 0.815 0.175 0.179],'String',...
    'Blue: Variant 1 Red : Variant
2','LineStyle','none','BackgroundColor','white');
a.FontSize=20;
```

FIGURE CAPTIONS

Figure 1: Phase diagram of enstatite (modified from Ulmer and Stadler, 2001 and Gasparik, 2014)). HCen refers to High-clinoenstatite, LCen to Low-clinoenstatite, Pen to protoenstatite and Oen to orthoenstatite. Dehydration conditions in the Cerro del Almirez serpentinite-metaperidote body (Padrón-Navarta et al., 2011) are indicated by the grey ellipsoid. Filled symbols are for Oen and empty symbols are for Cen. Composition of representative orthopyroxene used by Ulmer and Stadler (2001) to determine transitions between each phases is indicated. Orthopyroxene compositions in transitional lithology sample (T) and chl-harzburgite (G) from Almirez are also indicated.

Figure 2: (a) Sketches (Tröger, 1979) of orthoenstatite (Oen) and low-clinoenstatite (LCen) crystals. Orthoenstatite crystal with [100], [010] and [001] parallel to α, β and γ optical indicatrices, respectively, and optical axial plane (O.A.P) parallel to (001) in dashed lines. (b) Low-clinoenstatite crystal with [010] parallel to β, and γ at 32° from [001]. (c) Stereographic projection (lower hemisphere) of LCen illustrating the two transformation variants for the same orientation of Oen (with $[010]_{Oen}$ away from the viewer), associated shear senses and orientation of the maximum compressive stress.

Figure 3: Studied samples: Al10-10: antigorite-present transitional lithology sample, Al10-11: antigorite-absent chl-harzburgite, Al09-16: antigorite-absent chl-harzburgite with granofels texture. Note the bent of the foliation plane in Al10-11.

Figure 4: Comparison between measured (black circles) and calculated (white squares) LCen data for the antigorite-present sample AI10-10 and the antigorite-absent sample AI10-11. Note the agreement between the two datasets. Minor cases of disagreement are attributed to errors in the optical estimation of the transformation variant.

Figure 5: (a) Cross-polarized light image of a kinked Oen grain from AI09-16 sample with LCen lamellae (white thin bands). Extinction position of LCen lamellae changes abruptly at fold hinges indicating a change in transformation variant, which is confirmed by the change in the Kikuchi patterns in (d). Opposite shear sense assumed to have produced the two variants is indicated in the figure. (b) Misorientation map of the bent grain showing. Red star indicates reference point from which Euler angles are compared. (c) Band contrast image of the fold hinge zone with Bunge Euler colours for LCen lamellae. Note the change in orientation of the LCen lamellae. (d) Electron back-scattered diffraction pattern (Kikuchi bands) from Oen host and LCen lamellae. The main difference between the Oen host and the LCen lamellae is the 121 band, which is composed by multiple bands in Oen, but is single and thick in LCen, with asymmetric contrast for the two variants.

Figure 6: Crystallographic orientations of Oen and LCen in the antigorite-present sample AI10-10 (section A_1) and in the antigorite-absent sample AI10-11 (section A_1). (a) Oen orientations over the entire thin section. (b) LCen-bearing Oen. (c) Same projection than (c) but with variant 1 (black) and variant 2 (white) for measured (circles) and calculated (squares) data. LCen of variant 2 are distinct from LCen of variant 1. N indicates number of grains. The same reference frame for all projections

was used. Horizontal black thick line represents the foliation plane, which is vertical and oriented E-W. Projections are in lower hemisphere.

Figure 7: Histograms of distribution of angles between [010] axis and the thin section normal for LCen-bearing Oen.

Figure 8: (a) Crystallographic orientations of LCen lamellae calculated for thin sections A_2, B, and C of the antigorite-present sample Al10-10 and the antigorite-absent sample Al10-11. (b) Calculated orientation of the main compressional stress based on the entire LCen orientation dataset. (c) Sketch showing the orientation of A_2 (blue), B (red) and C (green) thin sections relative to the foliation plane and lineation. Filled markers represent variant 1 LCen and empty markers, variant 2. Squares represent calculated data and dots, measured data in A_1 section. N indicates number of data in each pole figure. Reference frame is the foliation and lineation of the serpentinite protolith, as in Figure 5.

Table 1: Number of LCen lamellae observed in each thin section and details of EBSD parameters used for spot analysis and orientation mapping of each sample. Only one value of MAD is displayed for A, B, and C sections of both samples because only Oen was analysed in these sections. See text for more explanations on EBSD parameters.

Table 1. Orthoenstatite (Oen) and low clinoenstatite (LCen) analyzed per section and details of EBSD settings used[a].

Sample	Al10-10 (antigorite-present				Al10-11(antigorite-absent)			
Section	A_1	A_2	B	C	A_1	A_2	B	C
Nb Oen	96	43	46	23	211	116	94	3
Nb Oen hosting LCen	11	7	1	6	76	34	3	3
Variant 1	7	3	0	3	50	14	1	1
Variant 2	4	4	1	3	26	20	2	2
% of Oen hosting LCen	11	16	2	26	36	29	3	100
Crystal Probe								
Exposure Time (ms)	175	132	132	132	175	131	395	395
MAD (LCen)	0.54	0.27	0.33	0.39	0.59	0.33	0.44	0.36
JEOL5600								
Exposure Time (ms)	12	21	21	21	12	20	21	21
Step Size (μm)	19	27	27	27	19	16	17	17

[a]Binning mode for Crystal probe is 2x2 (672x512 pixels) and for JEOL 5600: 4x4 (336x256) pixels)

Figure 1. Clément et al.

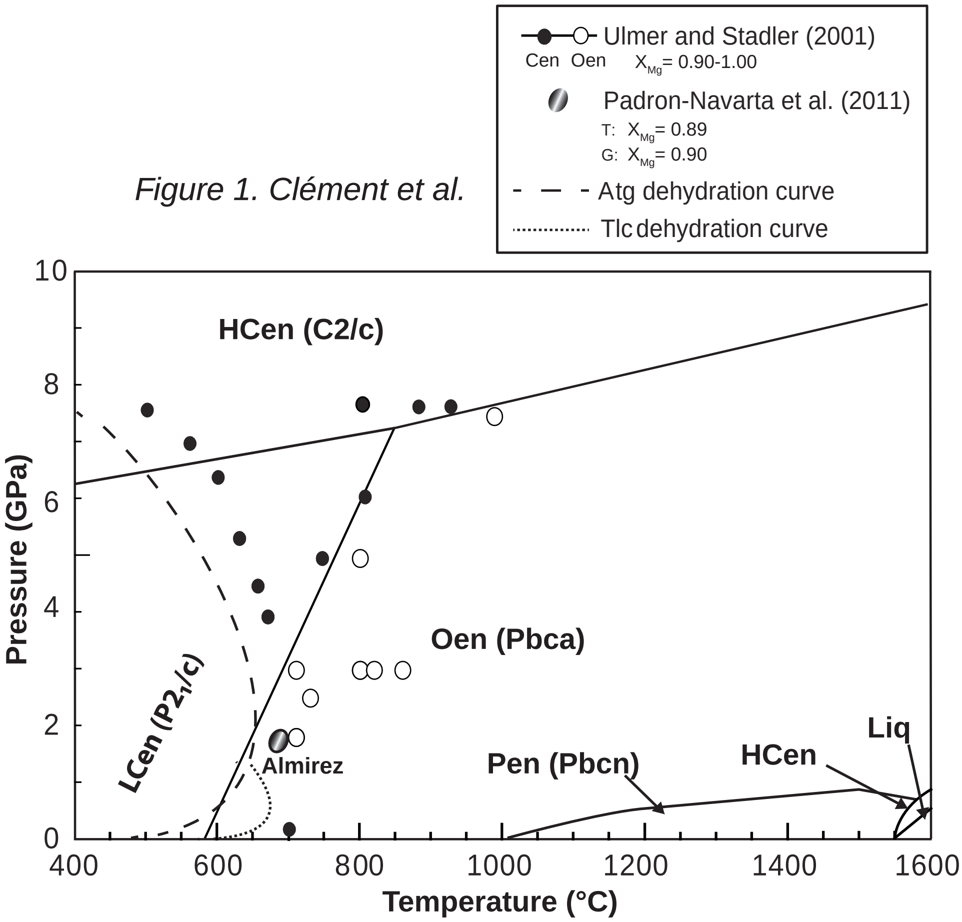

Figure 2. Clément et al.

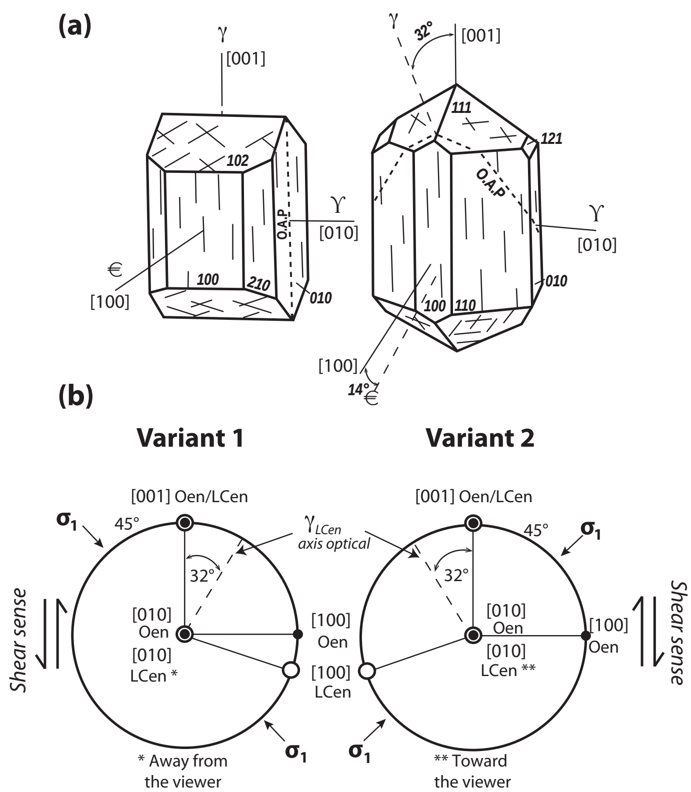

This is a preprint, the final version is subject to change, of the American Mineralogist (MSA)
Cite as Authors (Year) Title. American Mineralogist, in press.
DOI: https://doi.org/10.2138/am-2018-6362

Figure 3. Clément et al.

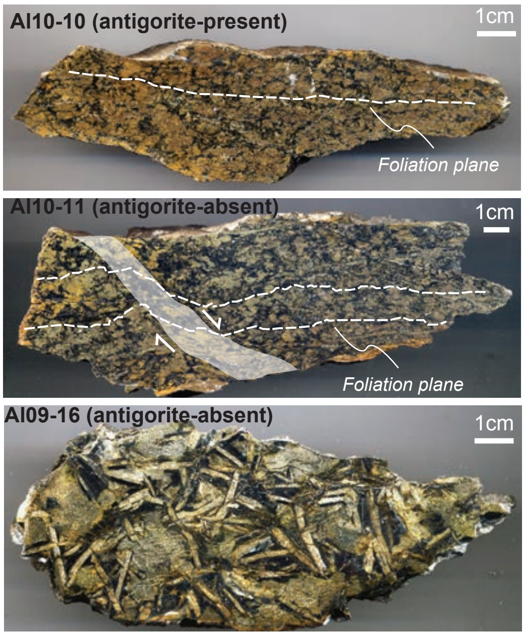

Figure 4. Clément et al.

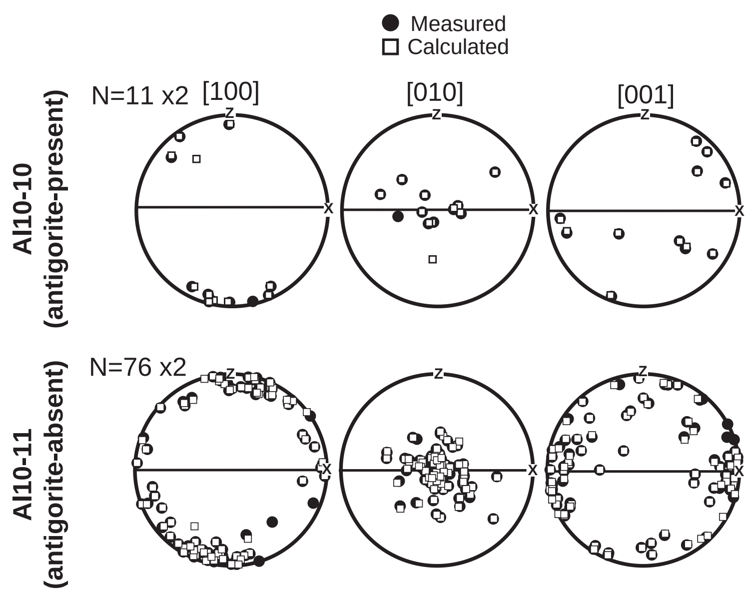

This is a preprint, the final version is subject to change, of the American Mineralogist (MSA)
Cite as Authors (Year) Title. American Mineralogist, in press.
DOI: https://doi.org/10.2138/am-2018-6362

figure 5. Clément et al.

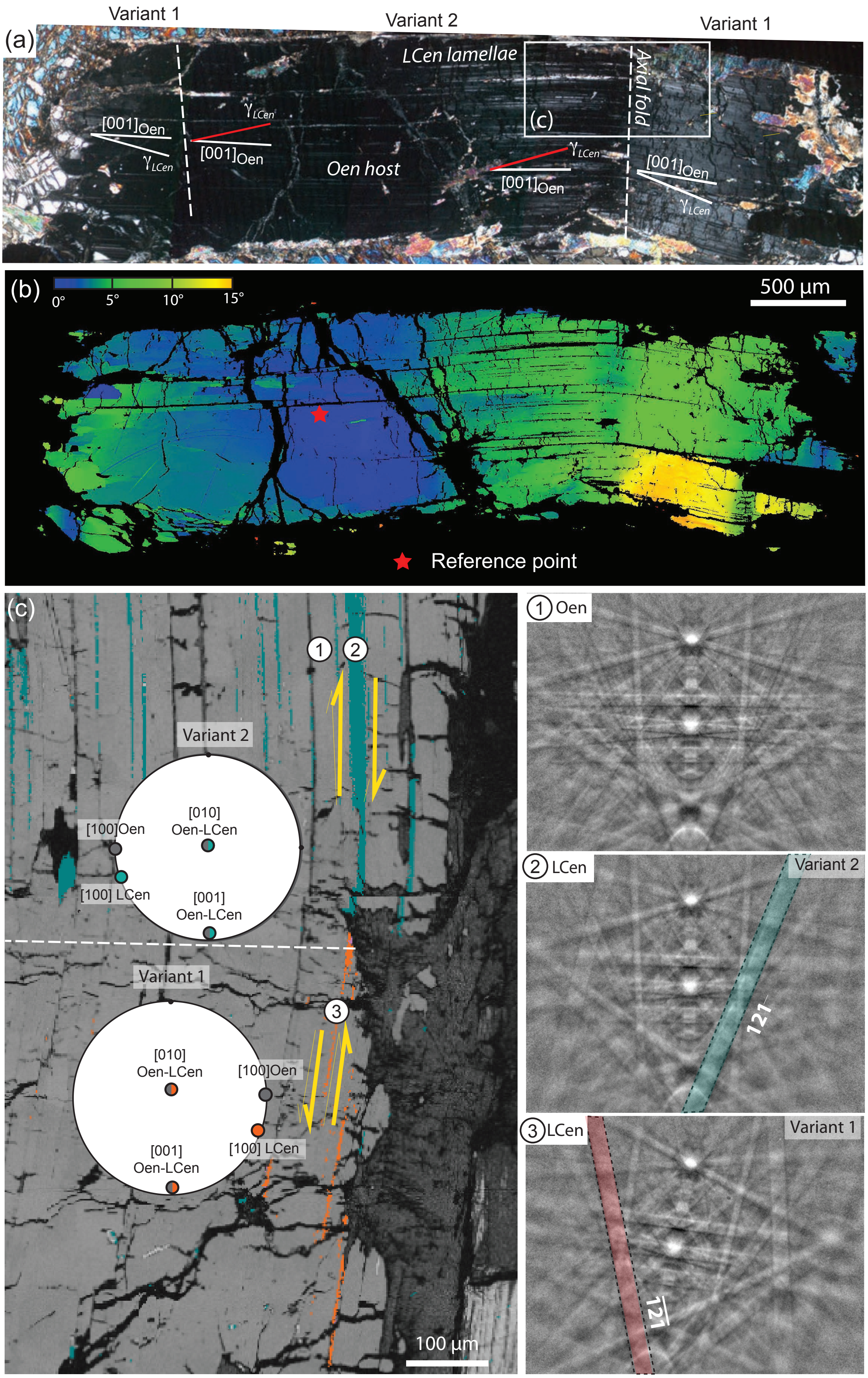

This is a preprint, the final version is subject to change, of the American Mineralogist (MSA)
Cite as Authors (Year) Title. American Mineralogist, in press.
DOI: https://doi.org/10.2138/am-2018-6362

Figure 6. Clément et al.

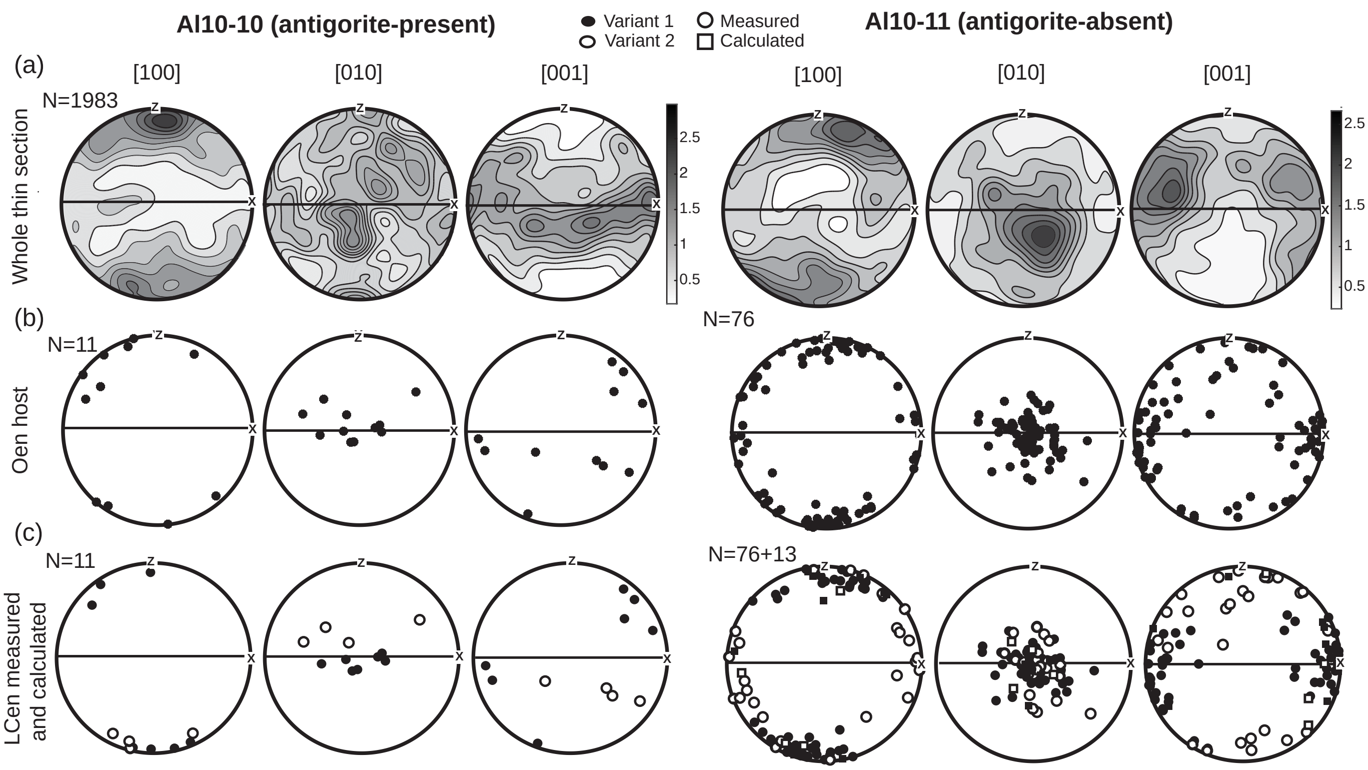

This is a preprint, the final version is subject to change, of the American Mineralogist (MSA)
Cite as Authors (Year) Title. American Mineralogist, in press.
DOI: https://doi.org/10.2138/am-2018-6362

figure 7. Clément et al.

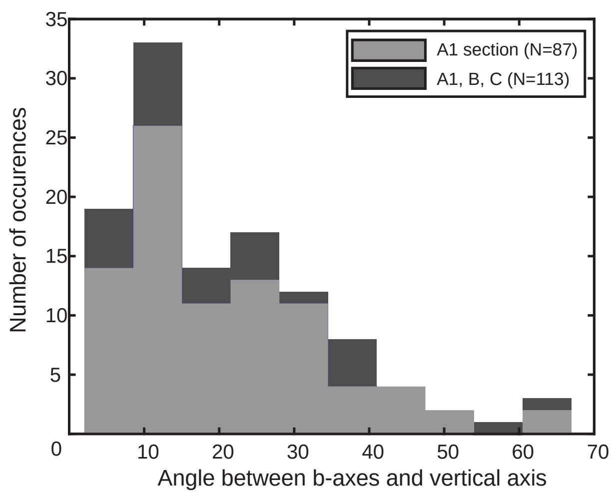

figure 8. Clément et al